Grain Boundary Feature and Its Effect on Mechanical Property of Ni 690 Alloy Layer Produced by GTAW

Wangteng Lin, Xiao Wei, Shaofeng Yang, Yuqian Huang, Maolong Zhang, Weihua Liu, Jijin Xu, Junmei Chen, Chun Yu and Hao Lu

Abstract Ni690 alloy surfacing layers were fabricated by gas tungsten arc welding (GTAW) with two different heat inputs, namely, large heat input (LHI) and small heat input (SHI). The high temperature performance of the surfacing layer was evaluated by employing Gleeble 3500 thermal/mechanical simulator. It is found that the ultimate tensile strength (UTS) of the LHI samples was higher than that of the SHI samples after reheat thermal cycles, regardless of the reheating temperature. The EBSD result shows that the proportion of high angle grain boundaries (GBs, >15°) in the LHI sample was obviously higher than that in the SHI sample. And more $M_{23}C_6$ particles were found to precipitate at the high angle GBs. The relations among UTS, GB angle distribution and $M_{23}C_6$ precipitations were analyzed. Moreover, the fracture modes were characterized by optical microscope (OM) and scanning electron microscope (SEM). The fracture mode was ductile fracture with deep dimples at 700 °C. While it changed to brittle intergranular fracture at 900 °C. As the temperature was enhanced to 1050 °C, the fracture returned to transgranular mode, with shallow dimples.

Keywords Nickel based alloy · Microstructure · Grain boundary precipitates Mechanical property · Welding

W. Lin · X. Wei · S. Yang · Y. Huang · M. Zhang · W. Liu
J. Xu · J. Chen · C. Yu (✉) · H. Lu (✉)
Key Lab of Shanghai Laser Manufacturing and Materials Modification, School of Materials Science and Engineering, Shanghai Jiao Tong University, Shanghai 200240, China
e-mail: yuchun1980@sjtu.edu.cn

H. Lu
e-mail: shweld@sjtu.edu.cn

M. Zhang
Shanghai Electric Nuclear Power Equipment Co., Ltd., Shanghai 201306, China

W. Liu
China Nuclear Industry Fifth Construction Co., Ltd., Shanghai 201512, China

S. Chen et al. (eds.), *Transactions on Intelligent Welding Manufacturing*,
Transactions on Intelligent Welding Manufacturing,
https://doi.org/10.1007/978-981-10-8330-3_8

1 Introduction

Ni-Cr–Fe alloys are widely used in manufacturing of nuclear power equipment (like steam generator tubes), because of its excellent corrosion resistance and high temperature performance [1]. 600 alloy, the content of Cr was 15%, was once selected as one of the nuclear power equipment materials [2], but it is easy to produce stress corrosion cracking (SCC), which is related to the poor Cr phenomenon near the grain boundaries (GBs). Then, 690 alloy (the content of Cr was up to 30%) was developed as a superior substitute material in pressurized water reactors (PWR) to avoid the SCC [3]. In practical engineering, multi-pass welding technology is often used, which is an essential process to fabricate the nuclear power application [4]. Lin [5] employed GTAW to study the relationships between microstructure and properties of buffer layer with Inconel 52M clad on AISI 316L stainless steel. And Lee and Chen [6] found that the phase transformations caused by the heat input in the traditional gas tungsten arc welding (GTAW) welding procedure. The heat affected zone (HAZ) should be subjected to at least two thermal cycles [7], which makes the microstructure of weldment more complex, further impacting the performance of welding joints [8]. Fink [9] used strain-to-fracture (STF) tests to investigate relationships between cracking morphology and metallurgical factors for Ductility-dip cracking (DDC) in the heat-affected zone(HAZ) of NiCr15Fe-type alloys. On other hand, it is well known that welding is a complex process which influenced by many parameters [10], especially, heat input is a key factor determining the performance and morphology of the weldment. Chen et al. [11] studied the effects of texture and grain boundary (GB) misorientation on liquation cracking susceptibility. They found that both liquation cracking and crystal misorientation were increased as increasing the heat input. Ma et al. [12] revealed that the carbide precipitation is a major microstructural characteristic during heat treatment of stainless steels and nickel-based alloys. And Lee et al. [13] identified the GB carbides in Inconel 690 tubes as chromium rich (Cr-rich) $M_{23}C_6$ carbide by employing selected area electron diffraction (SAED) pattern analysis. Meanwhile, Blaizot et al. [14] used EDX chemical measurement revealed that their composition is $Cr_{23}C_6$. Another important thing is that Trillo and Murr [15] assessed the sensitization and precipitation behaviors of $M_{23}C_6$ on GB by using the transmission electron microscopy (TEM). They found that a few small precipitates nucleated on small angle GBs in 304 stainless steels, while larger amount of carbides were observed on high angle GBs. Hence, they concluded that $M_{23}C_6$ precipitates were prone to nucleate at the high angle GBs because of the highest energy. Therefore, according to the above mentioned researches, the heat input may affect the $M_{23}C_6$ carbides precipitation, which deserve further research.

The elements have very important influence on the precipitation. For instance, it has been determined that Al and Ta alloying elements enrich interdendritic regions, while W, Cr, Mo, and Co are concentrated in the dendrite branches reported by Ospennikova et al. [16]. Wang et al. [17] reported that Cr-C co-segregation at grain boundaries induced the precipitation of chromium carbides $M_{23}C_6$. Moreover, as

the aging time was fixed, the GB precipitates $M_{23}C_6$ increased with the increase of GB angle. Since precipitations at GBs are important factor affecting the mechanical properties of metals [4], it is necessary to investigate the morphology, evolution process of precipitations at the GBs, as well as their effects on performance of metals. Especially, for Ni based alloys, which were usually served in high temperature, high pressure and corrosive atmosphere, their high temperature performance becomes more important. Moreover, due to alloying, precipitations at the GBs were the typical feature of the Ni based alloys, of course they had effect on performance of Ni based alloys. On other hand, during welding, the temperature field was not uniform, coupled with reheating cycle due to multi-pass welding, the microstructure, including the precipitations at the GBs, became more complex. Therefore, the evolution process of precipitations at the GBs of Ni based alloys with reheating thermal cycle needs to be well investigated, as well as its effect on mechanical properties.

In this study, hardfacing layers of Ni690 alloy were fabricated by gas tungsten arc welding (GTAW), with two different heat inputs, namely, large heat input (LHI) and small heat input (SHI). It is found that the microstructures of the two layers were different, especially, the proportion of high angle GBs (>15°) in the LHI sample was obviously higher than that in the SHI sample. And more $M_{23}C_6$ particles precipitated at the high angle GBs. The high temperature performance of Ni690 was investigated by employing Gleeble-3500 thermal/force simulation test machine. Microstructure was analyzed by optical microscope (OM), scanning electron microscope (SEM), and electron backscattered diffraction (EBSD). In particular, the influence of grain boundary precipitates $M_{23}C_6$ was investigated. The work provides the experimental and theoretical basis for the reasonable welding process of Ni690 alloy.

2 Materials and Experimental Procedure

The nominal chemical compositions in mass percent (wt%) of the deposited metal studied in this work are listed in Table 1. The metal was deposited on the base metal SA-508Gr.3Cl.1 by gas tungsten arc welding (GTAW). The welding parameters are shown in Table 2. The specimens for mechanical analysis were cut to tensile samples with thickness of 3 mm (Fig. 1), and the Gleeble-3500 thermal/mechanical simulation tester was employed to assess the mechanical properties at high temperature. Prior to thermal/mechanical tests, both sides of the specimens were pre-grinded till 400# abrasive paper. Then one side of the specimens was continually grinded till 2000# abrasive paper and polished with 5, 3, 1 μm diamond pastes in turn. After that, the sample thickness was reduced to about 2.8 mm. The process of high temperature tensile test was depicted in Fig. 2. After stretching at high temperature, the samples were chemically etched in 10% chromic acid solution for about 30 s with voltage of 12 V. Further, the surfaces were scrubbed with 2% dilute nitric acid corrosion, to remove the light-yellow corrosion layer. Then, the

Table 1 Chemical composition (mass percent) of deposited metal

Composition	C	Si	Mn	P	S	Cr	Ni
Content	0.03	0.26	3.99	0.005	0.0006	28.91	55.68
Composition	Mo	V	W	N	Al	Ti	B
Content	0.18	0.03	0.05	0.03	0.16	0.20	0.001
Composition	Co	Zr	Cu	Fe	Bi	Nb + Ti	Others (Co, B, Zr)
Content	0.03	0.003	0.03	8.79	0.001	1.60	0.08

Table 2 Welding parameters

No.	Welding parameters	Peak current (A)	Base current (A)	Duty cycle (%)	Welding speed (mm/min)	Wire feed speed (mm/min)	Welding voltage (V)
1	Large heat input (LHI)	250	180	40	140	1200	15–18
2	Small heat input (SHI)	300–320	240	40	150	1800	15–18

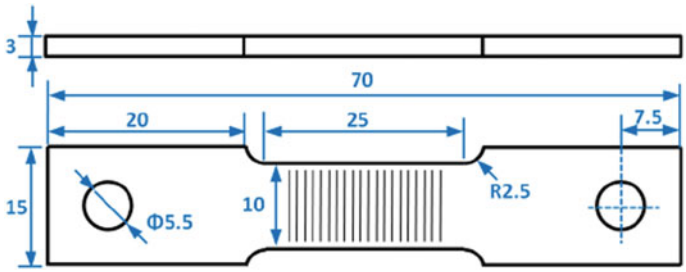

Fig. 1 Sketch map of high temperature tensile specimen

microstructures of the samples were investigated by using optical microscopy (AxioCam MRc5, Carl Zeiss) and scanning electron microscopy (NOVA NanoSEM 230, FEI). In order to analyze the GB angle distribution, the polished specimens were electro-polished in a solution of 10% $HClO_4$ + 90% CH_3COOH at room temperature with DC voltage of 15 V for 30 s, and characterized by electron backscattered diffraction (EBSD).

After reheating thermal cycle in Gleeble-3500 thermal/mechanical simulation tester, the tensile fracture surfaces were analyzed by using scanning electron microscope (SEM). And the microstructures of the specimen and morphologies of the $M_{23}C_6$ carbides were characterized in detail by OM and SEM.

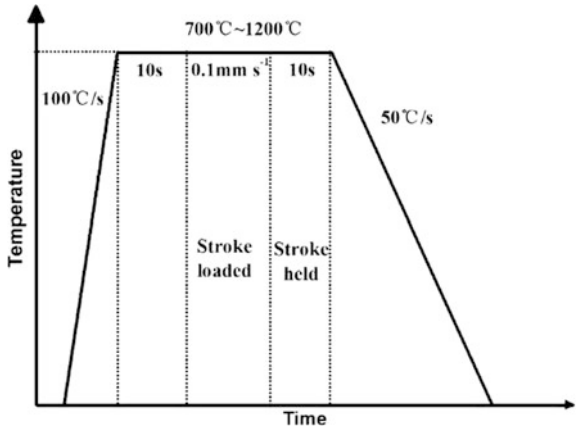

Fig. 2 Schematic diagram of high temperature tensile test

3 Results and Discussion

3.1 Influence of Heat Input in the Overlay Deposition

The supplied volume energy density E_v (in J/mm^3) can be used to evaluate the level of heat input for the cladding process, which plays a key role on the precipitations at GBs. The E_v that used by Yang et al. [18] is modified to measure average applied arc energy per unit volume during deposition:

$$E_V = \frac{U \times I}{S \times T \times V} \tag{1}$$

where U is the welding voltage (in V), I is the welding current (in A), S is the average pass space (in mm), T is the average thickness (in mm) of layer, and V (in mm/s) is the welding velocity. The area of layer was statistic by image J software, the calculated volume energy density E_v for large heat input (LHI) sample is about 559.65 J/mm^3. While for small heat input (SHI) sample, E_v is about 482.06 J/mm^3. Thus, the LHI deposition has a higher heat input per unit volume, relative to the SHI deposition.

3.2 Microstructure Characteristic of the as Surfaced Layers

Since the precipitations at GBs are affected by the high angle GBs, it is better to design samples with different high angle GBs. In this work, we found that the amount of high angle GBs can be changed by different heat input. Figure 3 depicts the results of EBSD characterization. EBSD inverse pole figure (IPF) maps observed from z direction show the grain crystallographic orientation and grain size

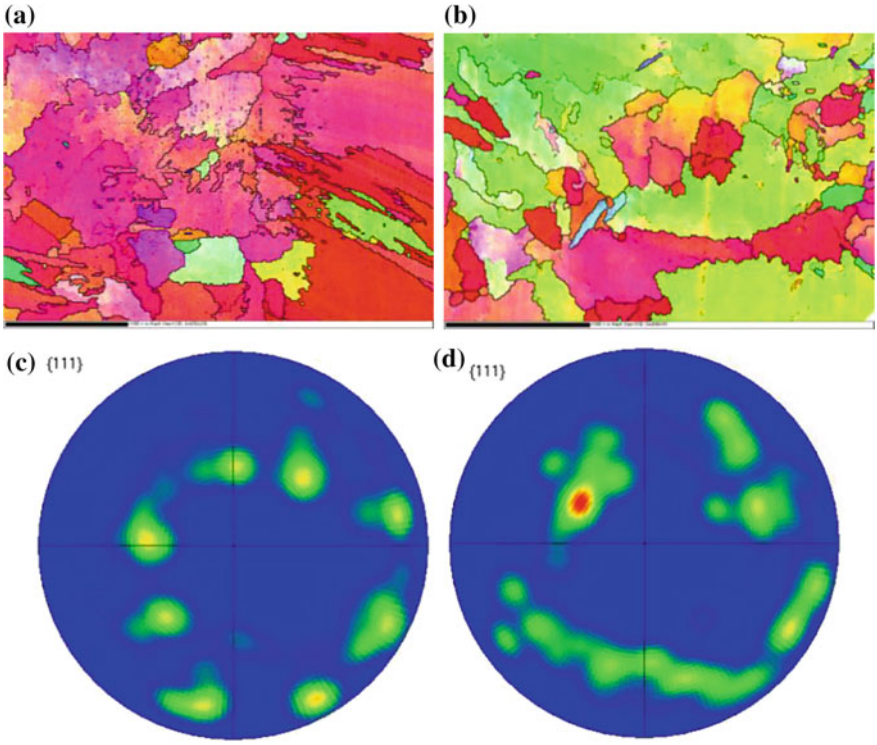

Fig. 3 Inverse pole figures (IPF) of **a** LHI and **b** SHI, corresponding pole figures (PF) of **c** LHI and **d** SHI

distribution. The pole figure (PF) in Fig. 3c, d indicates that orientation of the microstructure deviated from the <100> direction. And the grain orientation was more dispersed for the LHI sample.

The grain boundary angle distribution can be obtained from Fig. 4. It is found that there was obvious difference in the GB angle distribution. We divided the GB angle into three categories: <5°, 5–15° and >15°, which <5° was called as the small GB angle, the 5–15° was called as the middle GB angle, and that >15° was called as the high GB angle. There was no significant difference in the small GB angle and the medium GB angle. However, the proportion of high GB angle in the LHI samples was more than that in the SHI samples, as shown in Fig. 4. It is also proved that the heat input had a significant influence on the GB angle distribution [11].

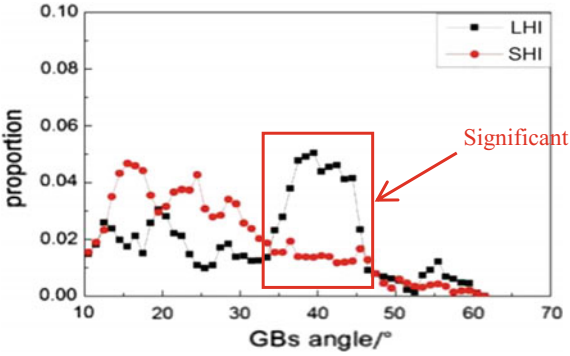

Fig. 4 Grain boundary angle distribution of parent material

3.3 *Effect of GB Carbides $M_{23}C_6$ on High Temperature Performance*

To investigate the effect of carbides on the high temperature mechanical property, the evolution process of precipitations at GBs was analyzed by SEM, the results were shown in Fig. 5. By using selected area electron diffraction (SAED) pattern analysis, Lippold and Nissley [7] detected chromium rich (Cr-rich) $M_{23}C_6$ carbides on the GBs of Inconel 690 Tubes. Moreover, the crystallography relationship between the $M_{23}C_6$ carbide and matrix was expressed as <100>$M_{23}C_6$//<100> matrix, {100}$M_{23}C_6$//{100} matrix [19]. It is seen that, according to Fig. 5a–c, the morphology of $M_{23}C_6$ in the LHI sample changed a lot after a high-temperature cycle. Continuous $M_{23}C_6$ distributed at the GBs as the reheating temperature was 700 °C, which almost fully covered the GBs, as shown in Fig. 5a. As the temperature was increased to 900 °C, $M_{23}C_6$ particles started to dissolve, and distributed semi-continuously, as shown in Fig. 5b. While as the temperature was 1050 °C, most $M_{23}C_6$ particles disappeared from the GBs, as shown in Fig. 5c. The results indicate that the amount of precipitations at GBs decreased with increase of reheating temperature. Figure 5d–f shows the $M_{23}C_6$ morphology in the SHI sample after a high-temperature cycle. The evolution process of precipitations at the GBs of the samples produced with SHI exhibited the similar rule, that is, the precipitations at GBs gradually dissolved with temperature increase at range of 700–1050 °C.

Meanwhile, according to the SEM photograph of GB, the amount of precipitates at the GBs of samples produced with LHI was much higher than those samples produced with SHI. For quantitative comparing the proportion of precipitates at GBs, image J software was employed. It can be seen from the Fig. 6 that the proportion of the GB precipitates in the LHI samples was 75%, and that in the SHI samples was about 49%, it is obviously lower than that of LHI samples. Moreover, this result is consistent with the comparison in the amount of the high angle GBs in the both samples produced with LHI and SHI, respectively. In other word, the GB $M_{23}C_6$ precipitates were more likely to precipitate at the high angle GBs. Lee et al.

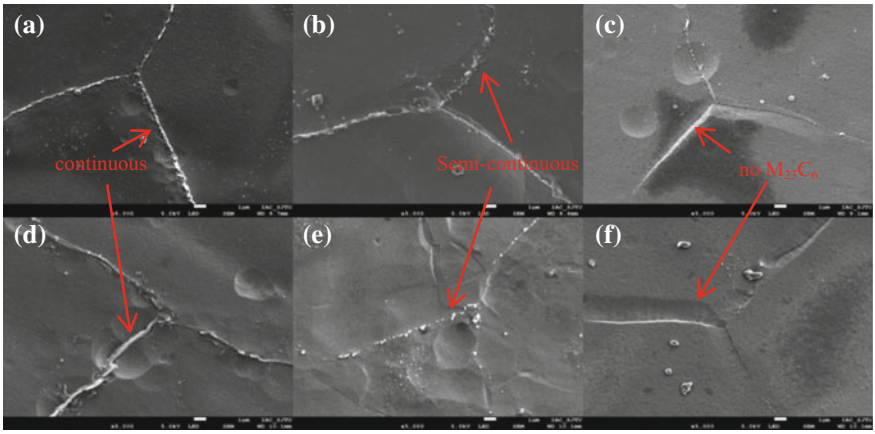

Fig. 5 Size and distribution of precipitates **a** LHI 700 °C; **b** LHI 900 °C; **c** LHI 1050 °C; **d** SHI 700 °C; **e** SHI 900 °C; **f** SHI 1050 °C

[13] also found that as the aging time was fixed, the GB precipitates $M_{23}C_6$ increased with the increase of GB angle. In this work, $M_{23}C_6$ was distributed in skeleton form at 700 °C, because the LHI samples had a large proportion of high angle GBs. The enhancement of the strength depends on the interaction of GBs, grain and GB $M_{23}C_6$ precipitates [10]. Moreover, $M_{23}C_6$ can effectively pin the GBs against migration, further improving the high temperature strength.

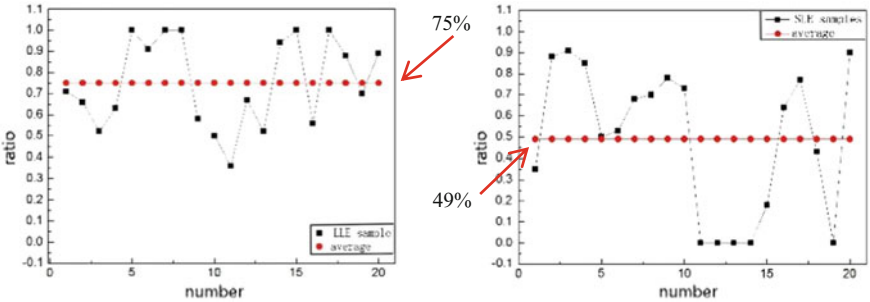

(a) LHI samples (b) SHI samples

Fig. 6 Grain boundary precipitation ratio of the as surfaced samples

3.4 Effects of Difference Heat Input on High Temperature Performance

Figure 7 plots the stress-strain curves of the samples during reheated to temperature of 700–1200 °C. It is found that, after yielding, the shape of stress-strain curve of the samples at 700 and 800 °C was very different from that at 900–1200 °C, regardless the heat input. The stress-strain curves of samples reheated to 700 and 800 °C exhibited a remarkable strain hardening feature. And they displayed a longer extension and abrupt fracture at last. However, the stress-strain curves of the samples after reheated to 900–1200 °C, leveled off after yielding, and elongation percentage was remarkably reduced, especially for the samples manufactured with SHI. There was a gradual fall in stress at the end of the tensile. The reason is that when the temperature was below 900 °C, the grain boundary strength was higher than that in the crystal, and the deformation was mainly concentrated in the crystal; however, when the temperature was higher than 900 °C, the grain boundary strength was weaker than the intragranular strength. At the same time, grain boundary sliding and dislocation climb became the main deformation mechanism [14].

Figure 8 presents the ultimate tension strength (UTS) as a function of reheating temperature. It is obvious that the high temperature UTS decreased with the increase of the reheating temperature. Moreover, the UTS of samples produced with LHI was larger than that with SHI at the corresponding reheating temperature. As can be seen from Fig. 8, the maximum UTS difference between two layers occurred at 700 °C, which was 33.79 MPa. However, the difference became smaller with the increase of temperature. As temperature ranging from 1000 to 1200 °C, the difference of the ultimate tensile strength value was not large.

Combining with the microstructure analysis, both the change of UTS with temperature, and the difference of UTS between different samples, had consistent trend with the evolution process of precipitates at the GBs. The amount of $M_{23}C_6$ at the GBs of LHI samples was higher than that of SHI samples, improving the effect of grain boundary pinning. Therefore, the ultimate tensile strength of LHI samples

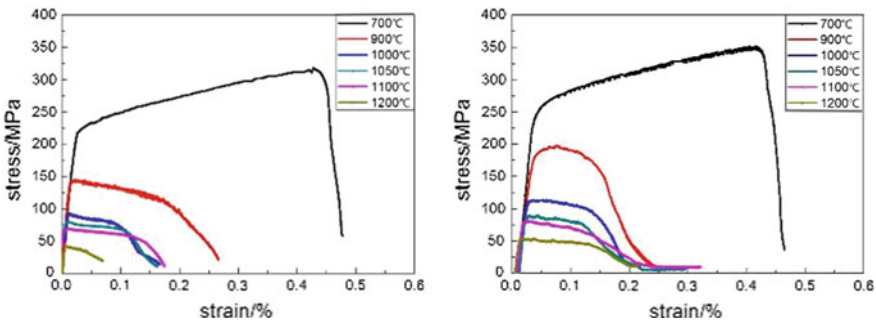

(a) LHI samples (b) SHI samples

Fig. 7 High temperature tensile stress-strain curves of LHI and SHI samples

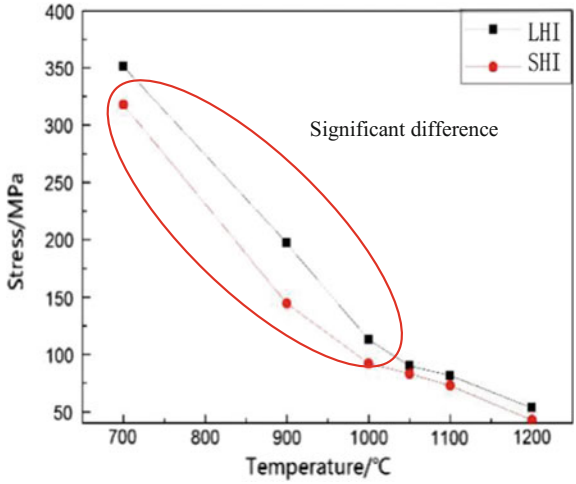

Fig. 8 Comparison of the ultimate tensile strength of LHI and SHI samples at various temperatures

was higher than that of the SHI samples. However, when the temperature was at the range of 1000–1200 °C, $M_{23}C_6$ had been dissolved into the matrix, which lead to the pinning effect on grain boundary be weakened, so it had little effect on the high-temperature ultimate tensile strength.

3.5 *Fracture Morphology Analysis*

The transverse section of the fracture was observed by the optical microscope, the samples which experienced reheating to 700, 900, and 1050 °C were selected to analyze the fracture characteristic. It is found that the fracture modes of the LHI samples were the same as the SHI samples, as shown in Fig. 9. As the reheating temperature was 700 °C, the failure occurred in a transgranular mode; as the reheating temperature increased from 900 to 1050 °C, the fractures for the high temperature tensile test turned from intergranular mode to transgranular mode. Previous research [20] had shown that when the temperature was between T_{E1} to T_{E2} (T_{E1}: 650–810 °C; T_{E2}: 870–930 °C), the GB strength was weaker than the intragranular strength, at this time, the fracture was transgranular brittle fracture. On the other hand, when the temperature was below T_{E1} or higher than T_{E2}, the grain boundary strength was higher than that of intragranular strength, which was intergranular ductile fracture.

Scanning electron microscopy (SEM) was used to observe the fracture morphology (700, 900, 1050 °C), and the fracture morphologies were shown in Fig. 10. It can be seen from Fig. 10a that the fracture surface exhibited a fine dimpled surface at 700 °C, which is the typical characteristic of the dimpled ductile mode of failure. It is attributed to the decrease of chromium concentration in the matrix which due to the coarse GB $M_{23}C_6$ carbides precipitated at the grain

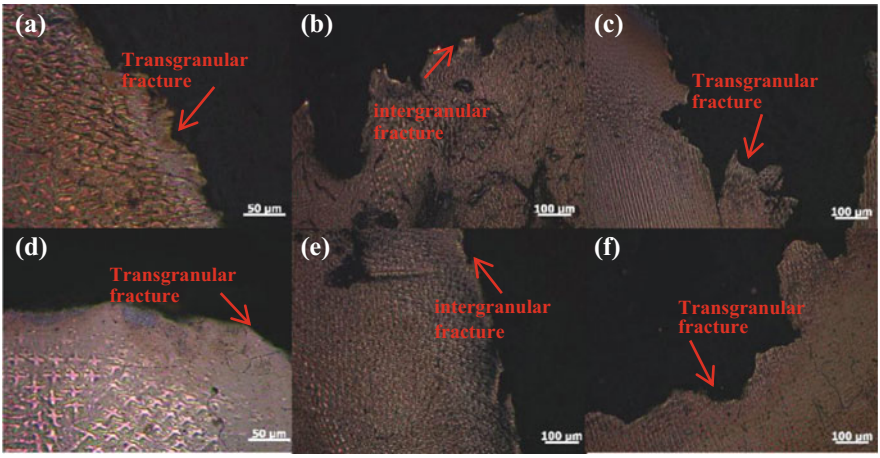

Fig. 9 Metallograph of the transverse section of the fracture **a** LHI 700 °C; **b** LHI 900 °C; **c** LHI 1050 °C; **d** SHI 700 °C; **e** SHI 900 °C; **f** SHI 1050 °C

boundary. It indicates that the strength of the GB was higher than that of the crystal due to the dislocation slipped to GBs; as temperature was 900 °C, it was brittle intergranular fracture, while dimple fracture disappeared. Meanwhile, the maximum strength difference between grain and GB was generated at 900 °C (Fig. 8), for which the fractures were entirely intergranular fractures (Fig. 10b, e). At this temperature, a higher content of $M_{23}C_6$ particles precipitated at the GBs (Fig. 5b, e). The intergranular fracture was caused by grain boundary embrittlement. As the temperature was 1050 °C, it was transgranular fracture and had many shallow dimples. Corresponding to the metallographic photograph (Fig. 9), the fractures of the high-temperature tensile test turned from dimple fractures to intergranular fractures at temperatures ranging from 700 to 900 °C, and then turned to dimple fracture again as the temperature continuously increased to 1050 °C. This result shows that the strength of the grain boundaries and crystal changed with the increase of temperature. At the beginning, the strength of the crystal was weaker than the GBs because of the precipitations, so the crack was easy to grow and expand in the crystal. Previous research had shown that when GB carbides in super alloys were continuously presented along the GBs, it would be deleterious to intergranular crack growth resistance [21]. With the increase of temperature, the strength of GBs decreased faster than that crystal due to dissolution and precipitation of precipitations, resulting in initiation of crack at GBs. As the temperature continued to rise, the intergranular carbides dissolved completely, leading the fractures turn to dimples, and the GBs strength is higher than that of crystal. Lee et al. [13] investigated the influence of GB precipitates behavior of Inconel 690 tube on tensile property, they found that $M_{23}C_6$ easily precipitated in the high angle GBs because of high surface energy. With the increase of aging time, the tensile strength and elongation decreased significantly. By analyzing the fracture surface, it is found that the precipitate $M_{23}C_6$ was the cause of crack initiation [20].

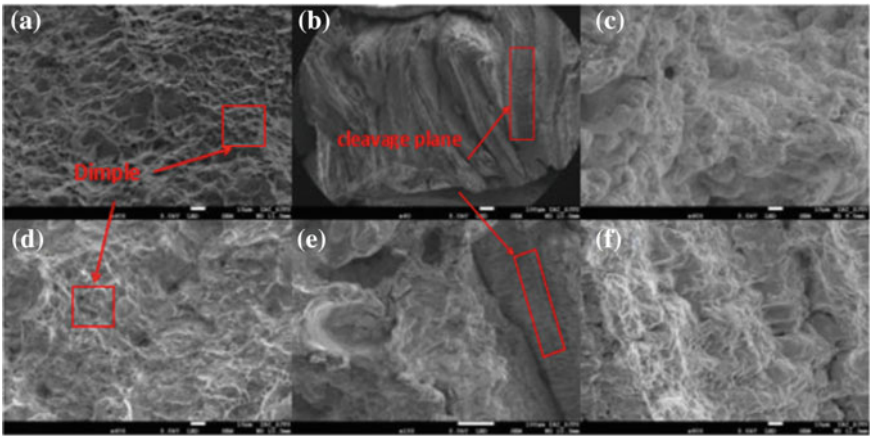

Fig. 10 Fracture morphology **a** LHI 700 °C; **b** LHI 900 °C; **c** LHI 1050 °C; **d** SHI 700 °C; **e** SHI 900 °C; **f** SHI 1050 °C

4 Conclusion

In present work, large heat input (LHI) and small heat input (SHI) were separately used to fabricate Ni 690 alloy hardfacing layer. The effect of GB angle and GB precipitates $M_{23}C_6$ on high-temperature performance were investigated. The major conclusions are listed as follows:

1. By changing the heat input, two kinds of hardfacing layer with obvious difference in grain boundary angle distribution were obtained. The samples produced with LHI had more large angle GBs than that produced with SHI.
2. The ultimate tensile strength of LHI samples was higher than that of SHI samples at the temperature range of 700–1000 °C. Moreover, it had significant difference at 700 and 900 °C. While as the temperature increased, the difference became smaller. At the range of 1000–1200 °C, the values of UTS were slightly different.
3. At 700 °C, continuous $M_{23}C_6$ particles distributed at the GBs, which almost fully covered the GBs; when the temperature increased to 900 °C, $M_{23}C_6$ became larger and dispersed at the GBs; while as the temperature was over 1050 °C, $M_{23}C_6$ particles dissolved. The evolution process of precipitations at the GBs of the samples produced with SHI and LHI exhibited the similar rule.
4. In SHI samples, the proportion of the large angle GBs was much higher than that of SHI samples, $M_{23}C_6$ was easier to precipitate at the large angle GBs. And the $M_{23}C_6$ at the GBs can effectively pin the grain boundaries against the migration, and improve the high temperature strength.
5. The fracture modes of the both samples were same: at 700 °C, it was transgranular fracture; at 900 °C, it was intergranular fracture; and at 1050 °C, it turned to transgranular fracture.

Acknowledgements The authors gratefully acknowledge the financial funding of the National Natural Science Foundation of China (51204107, 51575347 and 51405297).

References

1. Qin R, Wang H, He G (2014) Investigation on the microstructure and ductility-dip cracking susceptibility of the butt weld welded with ENiCrFe-7 nickel-base alloy-covered electrodes. Metall Mater Trans A 46(3):1227–1236
2. Lu Z, Chen J, Shoji T et al (2015) Characterization of microstructure, local deformation and microchemistry in Alloy 690 heat-affected zone and stress corrosion cracking in high temperature water. J Nucl Mater 465:471–481
3. Santra S, Rao Ramana, Kapoor K (2016) The effect of thermal treatment on microstructure and corrosion of nickel base Alloy 690 (UNS N0 6690). Mater Perform Charact 5(1):20160046
4. Chen JQ, Lu H, Cui W et al (2014) Effect of grain boundary behavior on ductility dip cracking mechanism. Mater Sci Technol 30(10):1189–1196
5. Lin CM (2013) Relationships between microstructures and properties of buffer layer with Inconel 52M clad on AISI 316L stainless steel by GTAW processing. Surf Coat Technol 228:234–241
6. Lee HT, Chen CT (2011) Predicting effect of temperature field on sensitization of alloy 690 weldments. Mater Trans 52(9):1824–1831
7. Lippold JC, Nissley NE (2008) Ductility-dip cracking susceptibility of nickel-based weld metals Part 1: strain-to-fracture testing. Weld J 87:257–264
8. Shen RR, Strom V, Efsing P (2016) Spatial correlation between local misorientations and nanoindentation hardness in nickel-base alloy 690. Mater Sci Eng, A 674:171–177
9. Fink C (2016) An investigation on ductility-dip cracking in the base metal heat-affected zone of wrought nickel base alloys—part I: metallurgical effects and cracking mechanism. Weld World 60(5):939–950
10. Zheng L, Hu X, Kang X et al (2015) Precipitation of $M_{23}C_6$ and its effect on tensile properties of 0.3C-20Cr-11Mn-1Mo-0.35N steel. Mater Des 78:42–50
11. Chen Y, Zhang K, Huang J et al (2016) Characterization of heat affected zone liquation cracking in laser additive manufacturing of Inconel 718. Mater Des 90:586–594
12. Ma Y, Li S, Hao X et al (2016) Research on the carbide precipitation and chromium depletion in the grain boundary of alloy 690 containing different contents of nitrogen. Acta Metall Sin 52(8):980–986
13. Lee T-H, Lee Y-J, Joo S-H et al (2015) Intergranular $M_{23}C_6$ carbide precipitation behavior and its effect on mechanical properties of Inconel 690 tubes. Metall Mater Trans A 46(9):4020–4026
14. Blaizot J, Chaise T, Nelias D et al (2016) Constitutive model for nickel alloy 690 (Inconel 690) at various strain rates and temperatures. Int J Plast 80:139–153
15. Trillo EA, Murr LE (1998) A TEM investigation of $M_{23}C_6$ carbide precipitation behaviour on varying grain boundary misorientations in 304 stainless steels. J Mater Sci 33(5):1263–1271
16. Ospennikova OG, Petrushin NV, Treninkov IA et al (2016) Phase and structural transformations in heat resistant intermetallide nickel-based alloy. Inorg Mater: Appl Res 7(6):832–839
17. Wang M, Zha X, Gao M et al (2015) Structure, microsegregation and precipitates of an alloy 690 ESR ingot in industrial scale. Metall Mater Trans A 46(11):5217–5231
18. Yang J, Li F, Wang Z et al (2015) Cracking behavior and control of Rene 104 superalloy produced by direct laser fabrication. J Mater Process Technol 225:229–239

19. Lim YS, Kim DJ, Hwan SS et al (2014) $M_{23}C_6$ precipitation behavior and grain boundary serration in Ni-based Alloy 690. Mater Charact 96:28–39
20. Mo W, Lu S, Li D et al (2014) Effects of $M_{23}C_6$ on the high-temperature performance of Ni-based welding material NiCrFe-7. Metall Mater Trans A 45(11):5114–5126
21. Defects W (2015) Effect of Nb content of Nb content on microstructure, welding defects and mechanical properties of NiCrFe-7 weld metal. Acta Metall Sin—Chinese Edition 51(2): 230–238